In vivo time-resolved echo-PIV measurement of cardiovascular flows with Extracorporeal Membrane Oxygenation

Zeng Zhang[1], Joseph Katz[1]*, Xun Zhou[2], Alejandro Suarez Pierre[2], Cecillia Lui[2], Sean Kearney[2], Enoch Yeung[2], John Young[3], Dan Choi[2]

[1]Johns Hopkins University, Department of Mechanical Engineering, Baltimore, USA

[2]Johns Hopkins Hospital, Department of Surgery, Baltimore, USA

[3]Johns Hopkins Hospital, Division of Pediatric Respiratory Care Services, Baltimore, USA

*katz@jhu.edu

Abstract

Extracorporeal Membrane Oxygenation (ECMO) is a life support technology used for patients with heart and lung failure by oxygenating the blood outside the body. The veno-arterial configuration is routinely used for providing both respiratory and hemodynamic support by delivering oxygenated blood through arteries and draining deoxygenated blood from the veins. However, the choice of the ECMO parameters, or the tradeoff between maintaining sufficient end-organ perfusion and reducing the afterload of the native left ventricle, is challenging without a non-invasive monitoring approach of the hemodynamics. Therefore, the current study applies PIV and PTV to determine the time-resolved velocity field from contrast-enhanced (micro-bubble seeded) ultrasonographic images in order to study the interaction between the cardiac flow of a severely injured pig's heart and the flow induced by an external ECMO machine. The measurements focus on the pig's aortic root, where the external ECMO flow impinges directly on the cardiac outflow. Prior to PIV/PTV analysis, image processing including blind deconvolution, and local background removal is performed to overcome the undesirable blur and to segment the bubble traces. In addition, active contouring is applied to define the boundaries of the aorta and the moving aortic valves. Phase-averaged vorticity field and velocity-time integral are presented to help estimate the transitional point, which is the divide between well-oxygenated ECMO flow and oxygen deficient cardiac flow, and the cardiac functions. The results suggest that for the present conditions, an ECMO flow rate of 3 L/min is optimal, under which the transitional point is located 0.8-1cm downstream the sinotubular junction, with a maximum cardiac ejection speed of 14 cm/s.

1 Introduction

Extracorporeal Membrane Oxygenation (ECMO) is a technology that can pump and oxygenate a patient's blood outside the body. There are two typical ECMO configurations: veno-venous (VV) and veno-arterial (VA). VV ECMO recovers respiratory function by draining blood from the vena cava or right atrium and returning to the right atrium (Makdisi et al. 2015), and VA ECMO provides both respiratory and hemodynamic support by draining blood through the venous system and returning through artery system (Pavlushkov et al. 2017). Therefore, VA-ECMO is often used as a salvage

therapy for patients with cardiogenic shock by offloading injured myocardium and thus favoring recovery (Lawler et al. 2015).

However, deciding optimal ECMO parameters, which involves the tradeoff between maintaining sufficient end-organ perfusion and allowing for myocardial recovery, is challenging. Because in the VA ECMO layout, the arterial cannulation delivers retrograde flow against the cardiac outflow, as illustrated in Figure 1. Therefore, higher ECMO flow, which is favorable for adequate perfusion, may increase the afterload against which the native left ventricle (LV) must eject and result in greater stroke work and myocardial demand (Ostadal et al. 2015), preventing cardiac tissues from recovery.

Monitoring hemodynamic changes using pressure catheters can help with deciding the right ECMO parameters. However, extra surgery is needed, and additional pain is caused on the patient during catheterization. Therefore, a reliable non-invasive test for identifying hemodynamic conditions associated with the myocardial recovery is required. The present study applies an integrated multiparameter echo PIV/PTV procedure (Sampath et al. 2018) to monitor the time-resolved cardiac flow field with various levels of ECMO flow rates. The echo-PIV was first introduced by Kim et al. (2003) for medical analysis, it has then been applied successfully to analyze abnormal LV flows over the last decade (Abe et al. 2013; Agati et al. 2014; Faludi et al. 2010; Sampath et al. 2018). Evolving from the optical PIV, echo-PIV uses ultrasonography for flow measurements in sample volumes without optical access. Contrast agents are administered intravenously as tracers. Typical contrast agents are lipid encapsulated perflutren microspheres with diameters ranging from 1-10μm that generate strong echo signals when excited at resonant frequencies.

In the previously successful applications of echo PIV in the human's LV, the regions of imaging are close enough to the ultrasound probe to maintain a satisfactory signal to noise ratio. In contrast, the current study focuses on the flow in the aortic root (AR) of a pig model. Since the orientation and depth of the pig's heart are different from those of human's, and the AR is sheltered by other ventricles, conventional Transthoracic Phased Array probes (TTE) are not suitable for the current study. Instead, a Transesophageal (TEE) Phased Array probe is applied for a closer look at the AR by performing observations through the pig's esophagus. Additional blind deconvolution (Pan et al. 2014) and local background removal procedures are introduced for deblurring the image and segmenting traces with spatiotemporal variant size and intensity distributions. Furthermore, an active contouring method is used to generate a specific mask for each phase in the cardiac cycle to accommodate the opening and closing motions of the aortic valve. The velocity field is calculated following the previous PIV/PTV procedure (Sampath et al. 2018) by choosing the optimized velocity vectors among those generated with varying enhancement parameters. The PIV measurements are then refined using the result by PTV and singular value decomposition (SVD) based interpolation. Phase-averaged vorticity distributions are used for demonstrating the changes to the flow field for varying ECMO flow rates, and for evaluating the transition point between well-oxygenated ECMO flow and oxygen deficient cardiac flow. The time integrals of velocity for each cardiac cycle as well as each minute are used for evaluating the cardiac function in response to different ECMO flows. Potentially, they could be used for choosing the optimal ECMO flow.

2   Methods

2.1 Experiment setup

Because of the similarities in cardiac output and blood circulation system, adult pigs (30±5 kg, cardiac output: 4L/min) are used as a model for human's blood circulation system in the current study. After the anesthesia, peripheral veno-arterial ECMO (VA ECMO) cannulation is implemented. As sketched in Figure 1, the return cannula, which sends oxygenated blood to the ascending aorta, is cannulated through the left femoral artery, and the drainage cannula, which drains deoxygenated blood from vena cava, is cannulated through the right femoral vein. This configuration bypasses both the lung and the heart to provide both respiratory and circulatory support (Pavlushkov et al. 2017). The other end of the drainage cannula is connected to a centrifugal pump which maintains the ECMO flow rate between 1.5L/min and 4L/min. The blood passes through an oxygenator and then flows back through the return cannula. Once VA ECMO cannulation is completed, a balloon is inserted in one of the left coronary arteries through the left femoral artery cannulation. The balloon is then inflated to cause ischemia in the muscles of the left ventricle. Depending on the extent of balloon inflation, a mild or a severe injury can be induced. The present study focuses on a severely injured model.

The contrast echocardiography is performed using the GE Vivid-E9 system. Since the orientation and the depth of the pig's heart are different from those of human's, the 6VT-D Transesophageal (TEE) Phased Array probe is used for acquiring data. Comparing with the conventional clinical Transthoracic Phased Array probes (TTE), which are placed against the chest, the TEE probe is placed in the pig's esophagus (Figure 1) closer to the region of interest (ROI). The current study focuses on the aortic root (at the bottom of the ascending aorta), where the outflow from the left ventricle and the retrograde ECMO flow impinge on each other. The images are acquired under the *Cardiac_E* factory presetting with harmonic imaging, and the mechanical index (MI) is adjusted to be lower than 0.4. The ultrasound beam sector is narrowed and tilted to focus only on the aortic root. The scanning depth is also tuned to bring the ROI to about 2/3 of the total depth for an optimal view. Under these settings, the current system can achieve a frame rate of 147 fps. For seeding the flow, 1.5ml of the contrast agent Definity™ (Bristol-Myers Squibb Medical Imaging, North Billerica, MA, USA) is diluted with 40ml saline and agitated gently to avoid sedimentation. For each recording, 2 ml of the solution is administered through the arterial cannula, and the cine loop is recorded for 15 cardiac cycles. The recorded data are written in a DICOM (Digital Imaging and Communications in Medicine) format with lossless RLE compression. The following image analysis steps of the cine clips are performed using an in-house echo-PIV code written in MATLAB on a desktop computer.

It is worth noting that routine contrast echocardiography is performed using the *Contrast* presetting, in which signals are acquired at a much lower overall MI. Hence, only the bubble traces can be seen in the recorded images. However, the *Contrast* mode is not ideal for an echo PIV study for the following reasons: 1) the *Contrast* mode works at lower frame rates. For a similar view of the current study, the *Cardiac_E* mode data can be recorded at 147 fps (or even more), but the *Contrast* mode data can only be acquired at 77 fps. 2) The choice of ROI depends on being able to obtain clear images of the boundaries between different chambers in the heart, and they are not observable in the *Contrast* mode images. It is also worth noting that clinical settings tend to involve significant levels of time averaging, spatial smoothing, and speckle removal, significantly reducing the ability to track individual bubbles. Hence, it is necessary to turn off all the smoothing functions while acquiring data for echo-PIV.
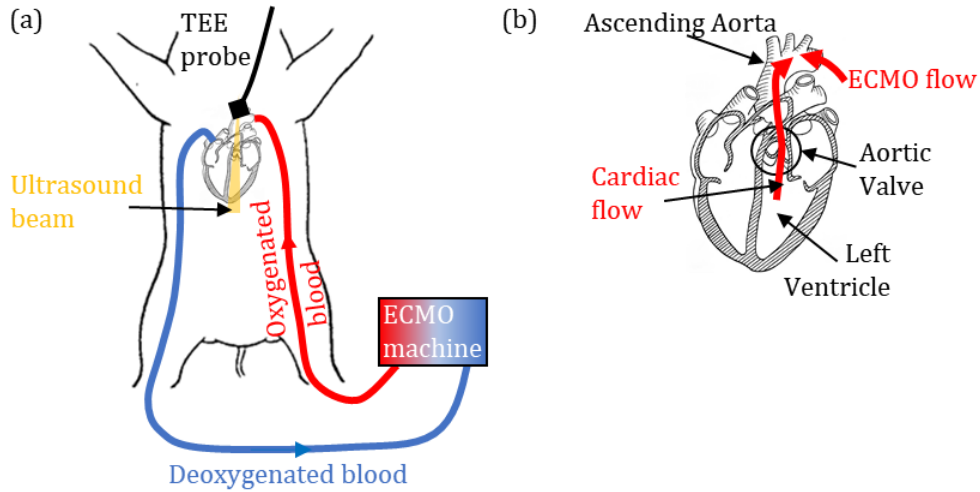
Figure 1: (a) the ECMO machine connected to the pig's heart and the location of the TEE probe for the present experiments, and (b) the sample area focusing on the LV and the ascending aorta.
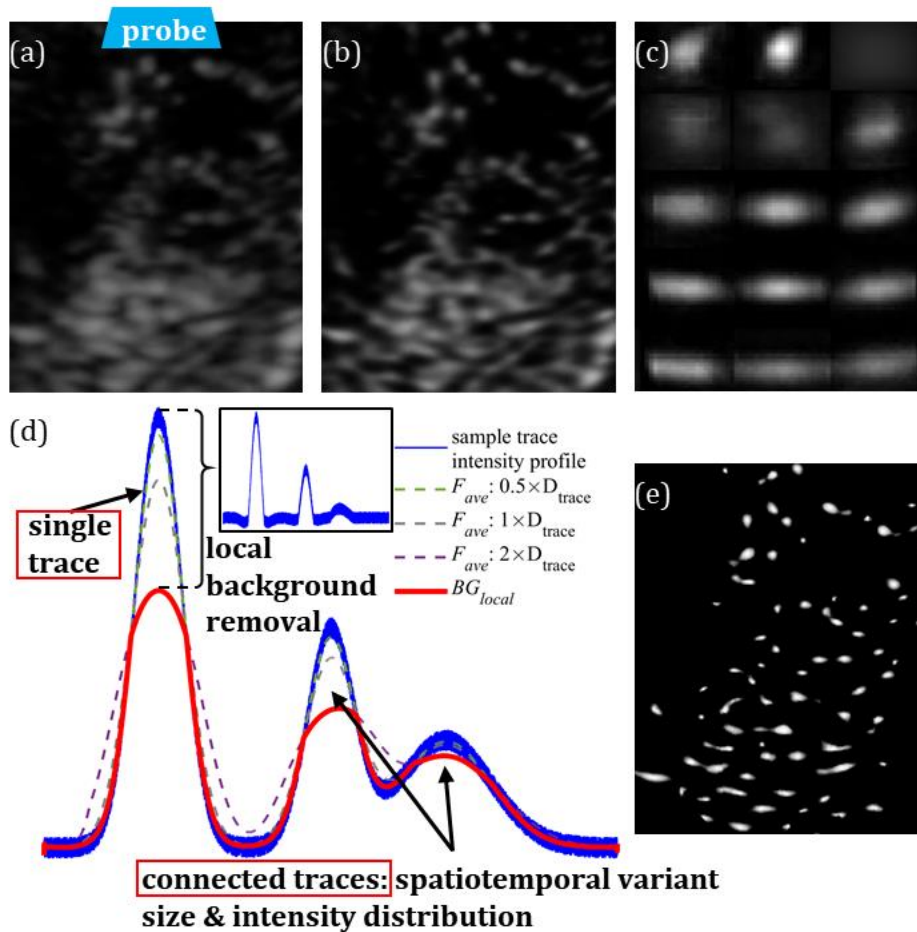
2.2 Image preprocessing

Figure 2: Image processing procedures: (a) sample raw image, (b) image after blind deconvolution, (c) the spatially variant point spread functions, (d) sample trace intensity profile showing: left -

typically isolated traces; right - aggregated traces with various size and intensity distribution, and (e) image after enhancement.

2.2.1 Blind deconvolution

Several mechanisms affect ultrasound image quality. First, due to the considerable range of penetration depths and the varying layers of tissues between the ultrasound probe and the regions of interest (ROI), the ultrasound wave and its echo attenuate in different levels spatiotemporally, resulting in varying tracer intensities (Fig. 2(a)). For similar reasons, the noise caused by echoes from tissues or other traces is also prone to a non-uniform spatiotemporal distribution. Second, the curvilinear scanning mechanism of the ultrasound beams tends to produce increasingly elongated traces with increasing distance from the probe. Finally, the spatial distribution of the traces, which is determined by the blood circulation, is usually not uniform. Though less apparent in previous human subject LV studies because of the closer distance between the apex 4 chambers (A4C) view and the ultrasound probe (Abe et al. 2013), these issues are inevitable in the current measurements on the pig's aortic root with more tissues to penetrate. As shown in Fig. 2(a), the traces, especially those at the bottom of the image, which are located farthest from the probe, have been deteriorated to a nearly uniform intensity distribution with obscure boundaries between them. Consequently, segmentation of individual traces required for the PIV/PTV procedure is hard and subject to inaccuracies. Therefore, additional image preprocessing is carried out for deblurring and denoising the current echo images.

Since the diameters of the current traces are usually around 3μm (Goertz et al. 2007), which is lower than the spatial resolution of the imaging system, these tracers act as point scatterers with uniform peak intensity (I_{uni}) that appear being blurred differently in the image. The shape and the intensity of the blurred signals are affected by the local blurring kernels or the point spread functions (PSF). Therefore, the acquired raw image (I_{raw}) could be modeled as the convolution between the PSF and I_{uni} with additional noise:

$$I_{raw} = PSF \otimes I_{uni} + n \tag{1}$$

The PSF is usually unknown. Viessmann et al. (2013) apply an *in-vitro* model with a thin wire to estimate the PSF of the echo images at a certain depth. This approach might not be sufficient for deblurring images recorded in clinical studies, where the PSF varies spatially because of the curvilinear scanning on a broad range of depth. Therefore, the current study applies the blind deconvolution algorithm proposed by Pan et al. (2014) to estimate the PSF. The PSF is evaluated by alternately and iteratively solving:

$$min_{(I_{uni})} \|I_{uni} \otimes PSF - I_{raw}\|_2^2 + \beta\|I_{uni} - u\|_2^2 + \mu\|\nabla I_{uni} - g\|_2^2 \tag{2}$$

$$min_{(u)} \beta\|I_{uni} - u\|_2^2 + \lambda\sigma\|u\|_0 \tag{3}$$

$$min_{(g)} \mu\|\nabla I_{uni} - g\|_2^2 + \lambda\|g\|_0 \tag{4}$$

and

$$min_{(psf)} \|\nabla I_{uni} \otimes PSF - \nabla I_{raw}\|_2^2 + \gamma\|PSF\|_2^2 \tag{5}$$

In which, Y, λ, and σ are the input weights. u and g are auxiliary variables corresponding to I_{uni} and ∇I_{uni}. β and μ are initiated with $2\lambda\sigma$ and 2λ accordingly and multiplied by 2 for each step until a prescribed limit. The choice of the blind deconvolution parameters in the current study follows the suggested values by Pan et al. (2014). Using search windows containing 5 to 10 traces in searching steps of half the window width, the process is carried out separately for each window. Twenty random images are selected for PSF estimation, and the results are averaged and subsequently used as the PSF for deblurring the rest of the images. The PSFs obtained at different locations for the present data are shown in Fig. 2(c). As is evident (and expected), with increasing distance from the ultrasound probe, the peak intensity decreases, and traces become more stretched and blurred. Using these PSFs and applying a deconvolution algorithm (Whyte et al. 2014) with saturation suppression result in the deblurred image (I_{deconv}) shown in Fig. 2(b). The intensity peaks in the center of each trace are more prominent, and the boundaries between adjacent traces are much clearer, facilitating the following image enhancement procedures.

2.2.2 Image enhancement

The purpose of the image enhancement is to separate the traces from the noisy background as well as remove other objects, such as aortic valve leaflets, walls of the ascending aorta, and other tissues. These tissues appear as large patterns, which are either stagnant or located at similar places at the same phase for each cardiac cycle. Therefore, as a first step, a phase is assigned to each image based on the Electrocardiogram (ECG). The peak of the P wave, which is conventionally defined as the beginning phase of the cardiac cycle, is hard to track on the ECG signal shown on the echo images. Hence the current study uses the peak of the R wave as the beginning phase of the cardiac cycle. The average (I_{ph}) and the standard deviation (σ_{ph}) of all the I_{deconv} at each phase are calculated to estimate the background and location of the tissues. For each phase, a threshold T_σ for σ_{ph} is computed using Otsu's thresholding method (Otsu 1979) to identify the slowly moving or stagnant regions for each phase, which usually correspond to tissues. The pixels whose $\sigma_{ph}(i,j)$ is smaller than $0.2T_\sigma$ are first removed, and I_{ph} is then subtracted from I_{deconv} for each phase. After the background subtraction, the noise is mostly removed, but the images are still not ready for the PIV/PTV procedure for two reasons: 1) the aggregated traces are not sufficiently separated, as sketched in Fig. 2(d), and 2) the signatures of the tissues are not entirely removed as their intensities vary over time.

To address the first problem, additional local background subtraction is performed. After the phase-average-subtraction, the remainder image (I_{sub}) features a non-uniform spatial distribution of trace intensity and size, and a lower noise level. Simply imposing a universal threshold to separate aggregated traces may also remove dim isolated traces. Therefore, the background removal is carried out locally. Six 2D moving average operators (F_{ave}) with window sizes ranging from $0.5D_{trace}$ to $2D_{trace}$ are applied to the I_{sub}, where D_{trace} is the estimated trace diameter. Using a range of filter sizes is aimed at accommodating varying trace sizes across the image. This filtering procedure produces six different filtered images (I_{filt}). As demonstrated in Fig. 2(d), the minimum value at each pixel among these six values of I_{filt} is the estimated local background. By subtracting this estimated local background, the aggregated traces can then be segmented by applying a universal threshold (Fig. 2(d)).

For the second problem, an active contour approach (Chan et al. 2001) is utilized to generate a different mask for each phase automatically. This algorithm is designed to segment the input image

into disconnected foreground and background of low intra-region variance, which are separated by a smooth closed contour (Maska et al. 2013). The algorithm solves the minimization problem of a morphology regularized energy function by re-expressing it using a level set formulation (Osher et al. 1988), and then obtaining the steady-state solution of the associated Euler-Lagrange equation iteratively. The entire process is illustrated in Figure 3. Since the solution of this algorithm tends to converge on the sharp local edge or corner features, the current study first stretches the contrast of each I_{ph} using:

$$S_{ph} = \frac{1}{1 + \left(\frac{I_{ph}}{\overline{I_{ph}}}\right)^5} \qquad (6)$$

where S_{ph} and $\overline{I_{ph}}$ are the contrast-enhanced image and the average intensity of each I_{ph}, respectively. The valve region is treated separately using a similar approach and integrated back into S_{ph}, as shown in Fig. 3(b). Furthermore, a rough mask is generated manually based on the ensemble averaged image of I_{deconv} to confine the solution to the region of interest (Fig. 3(c)). For clarity, the boundary of the mask is marked in Figure 3 in yellow, inside which is the ROI of the current study. For the next step, an initial guess of the mask is created manually, and the same initial mask is applied to all the I_{ph} (Fig. 3(d)). The active contour algorithm is then executed to generate a specific mask for each I_{ph}. The current method allows using an initial mask in random sizes. To speed up the convergence, it is suggested to use a very close guess as the initial mask. As demonstrated in Fig. 3(d-f), the contour gradually converges to the enhanced boundary features with iterations. For the current study, it usually takes 200 steps for the mask to converge.
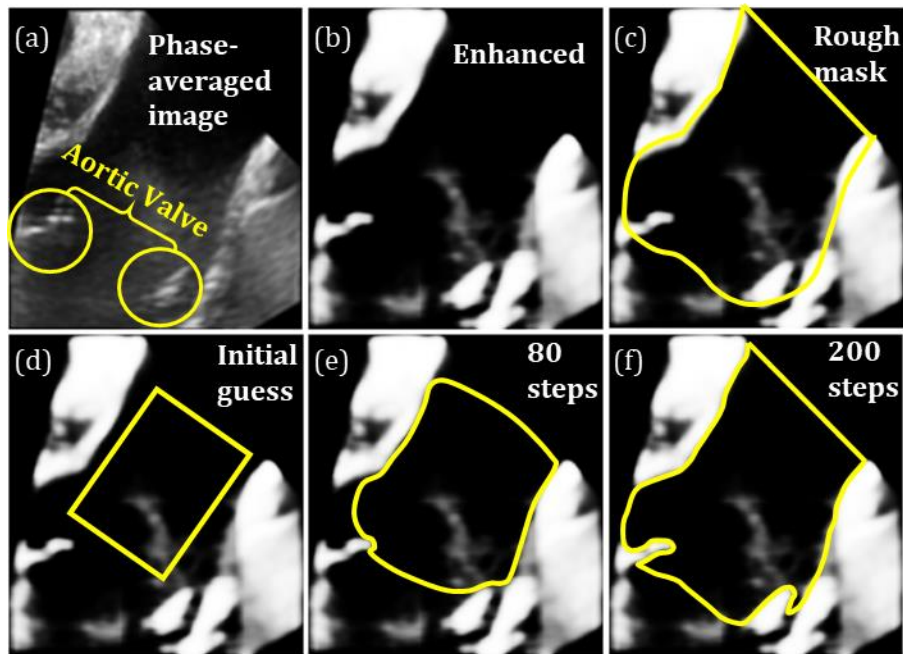

Figure 3: Active contouring procedures: (a) phase-averaged image showing the aortic valve leaflets and the walls of the ascending aorta that need to be masked out, (b) image after intensity stretching and valve specific enhancement, (c) the rough mask (yellow curve) generated manually using the ensemble-averaged image and applied to (b), (d) initial guess for the active contour algorithm

(yellow rectangular), (e) mask produced after 80 iterations (yellow curve), and (f) final mask created after 200 steps iterations (yellow curve).

The local background removal and phase-specific masking are applied to every I_{deconv}. Then, taking advantage of the intensity peaks in the center of traces and steep gradient along their boundaries, intensity and gradient thresholds, followed by a modified histogram equalization (MHE)(Roth et al. 2001), are imposed to enhance the remaining traces, obtaining the image shown in Fig. 2(e). The choices for the intensity, gradient, and MHE thresholds follow the previous work described in Sampath et al. (2018).

The PIV analysis is performed following the procedures described by Sampath et al. (2018). The parameters for PIV computation, namely correlation threshold, allowed variation between neighboring vectors, and window size, are hard to preselect due to the nonuniform trace density. Hence, a parameter space, which includes both the image enhancement and PIV parameters, is created. Standard correlation-based analysis performed for each parametric combination resulting in a corresponding velocity distribution. Subsequently, an optimization procedure, which includes outlier removal and smoothing, is applied to select the correct vector among the different parametric combinations. It is followed by a super-resolution PIV procedure (Keane et al. 1995), which is based on particle tracking and guided by the optimized PIV data. In searching for the correct candidates, a series of properties including deviation from the expected locations, percentage change in the area and perimeter, data continuity and peak cross-correlation values are imposed. Then, singular value decomposition (SVD) (Sheng et al. 2008) is used for interpolating the PTV data onto a regular grid, and integrating it with the PIV results. Details on these procedures are provided in Sampath et al. (2018).
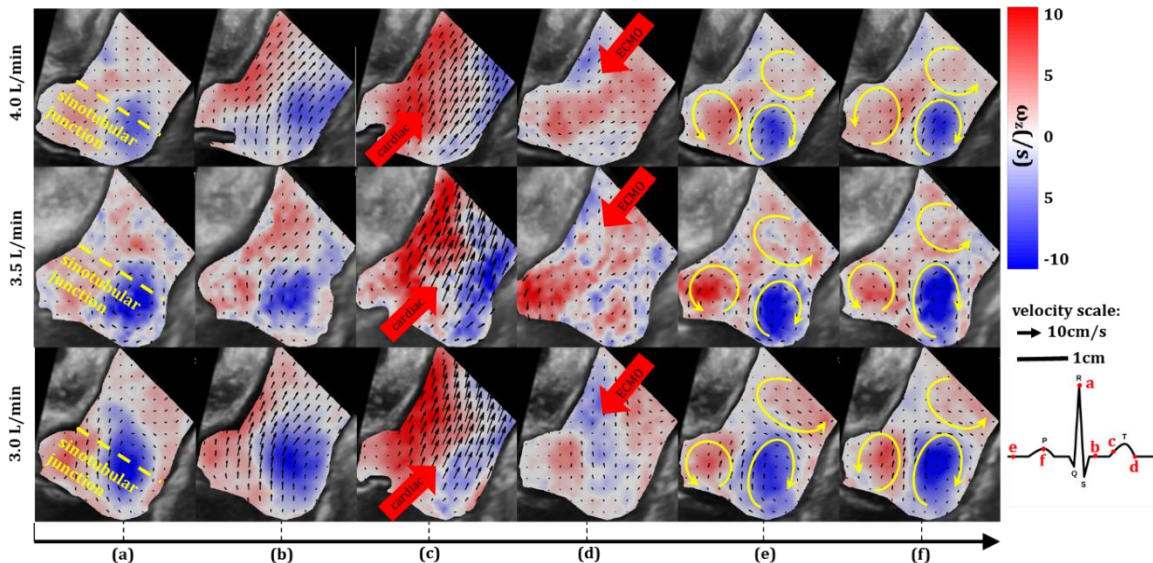
3   Sample Results

Figure 4: Phase averaged vorticity (color contours) and velocity (arrows) for ECMO flows of 4.0 (top row), 3.5 (middle row), and 3.0 L/min (bottom row). Sample phases shown are: (a) peak of the R wave, the selected initial phase, (b) aortic valve opening, (c) intermediate phase of the ventricle systole, (d) aortic valve closing, (e) intermediate phase of ventricle diastole, and (f) peak of the P wave.

To maintain adequate perfusion for the current severely injured heart, the data acquisition is performed starting from high ECMO flow rates, 4.0 L/min. The flow rate is then carefully lowered in steps of 0.5L/min until it decreases to 1.5 L/min. Figure 4 shows sample contour plots of the phase-averaged vorticity field for ECMO flows of 3.0, 3.5, and 4.0 L/min, each calculated based on data recorded over 10 cardiac cycles. Retrograde ECMO flows right before valve closing are observed for all three cases, as highlighted by the arrows in phase d. Before valve opening, as the ECMO flow keeps perfusing the ascending aorta, interactions with secondary flows remaining from the previous cardiac cycle result in the generation of a pair of counter-rotating vortices inside the sinus (phases e, f and a). The peak vorticity magnitude appears to increase with decreasing ECMO flow rate. Once the LV pressure (P_{LV}) surpasses the aortic pressure (P_{AR}), the aortic valve opens, and the LV flow forms a strong ejection (phases b-c), forcing the ECMO flow away from the valve. As the ECMO flow rate decreases from 4.0 to 3.0 L/min, the maximum ejection velocity increases from 12 to 14cm/s, and the location of maximum ejection speed in the sample area migrates 0.5cm downstream. These trends are consistent with the expected improvements to cardiac function with decreasing ECMO. As the aortic valve closes, there is an immediate reversal of the flow direction along the upper wall of the ascending aorta (phase d). This reverse flow generates an outwards flow along the lower wall of the aorta, and a region with positive vorticity 0.8-1cm downstream the sinotubular junction. Subsequently, the ECMO flow turns away from the valve (at least in the present plane), and a pair of counter-rotating vortices form immediately downstream of the valve, with the negative vortex located at the right bottom corner of the sinus. This pair stays at a similar location until the next cardiac outflow (Fig. 4(e-f)). In general, it appears that for ECMO flows above 3.0 L/min, the transition between this vortex pair and the ECMO backflow is located 0.8-1 cm downstream the sinotubular junction.
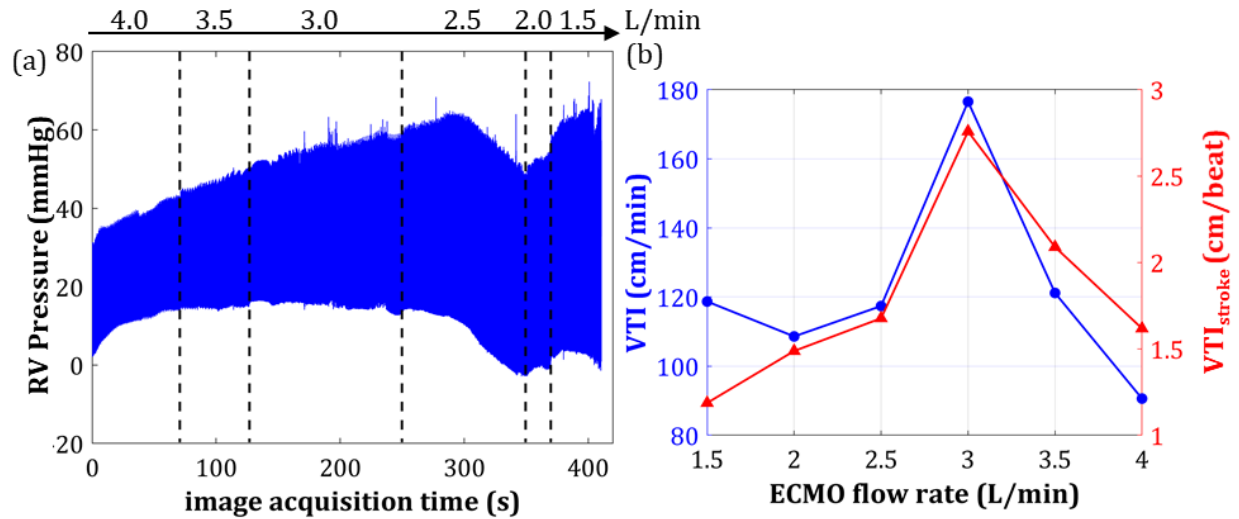

Figure 5: (a) Right ventricle pressure signal indicating heart failure at 2.5 L/min, and (b) velocity-time integral during systole per minute (*VTI*, left axis) and per stroke (*VTI*$_{stroke}$, right axis).

To evaluate the cardiac function as a function of ECMO flow rate for the current severely injured heart, we calculate the velocity-time integral across a cross-section located 1cm downstream the sinotubular junction and aligned nearly perpendicularly to the aortic walls by:

$$VTI_{stroke} = \sum_{systole} \overline{v_{out}} \times \Delta t \qquad (7)$$

$$VTI = HR \times VTI_{stroke} \qquad (8)$$

Here, HR is the heart rate, Δt is the time lag between phases, and $\overline{v_{out}}$ denotes the cross-sectional average velocity, which is a surrogate for the cross-sectional flow rate. Although the locations of the views are consistent for all the cases, they are not precisely aligned to the center plane of the ascending aorta. Therefore, $\overline{v_{out}}$ is used directly instead of multiplying it by an area estimated from the length of the sinotubular junction to avoid confusing the actual total output flow rate from the LV. Summing the values of $\overline{v_{out}} \times \Delta t$ during systole per each cycle represents the cardiac output or the stroke volume per unit area of the aorta per cycle, which is noted as VTI_{stroke} (right axis of Fig. 5(b)). Multiplying VTI_{stroke} with HR represents the overall cardiac output per unit area of the aorta and is noted by VTI (left axis of Fig. 5(b)). According to published pressure-volume loop simulation (Burkhoff et al. 2015), a healthy active hemodynamic response shows an increasing stroke volume as the ECMO flow decreases. The plot of VTI_{stroke} vs. ECMO flow rates in Fig. 5(b) shows a similar trend, i.e., VTI_{stroke} increases from 1.6 to 2.75 cm/beat when the ECMO flow decreases from 4.0 to 3.0 L/min. This trend suggests that in that period, the ECMO flow is sufficient to maintain adequate perfusion of oxygenated blood in the coronary arteries, resulting in the expected response to the decreasing ECMO flow. However, there is a sharp drop in VTI_{stroke} as the ECMO flow rate is decreased to 2.5 L/min or lower values. In this range, the heart no longer responds significantly to the variations in ECMO flow. Since the current heart is severely injured, we speculate that a 2.5 L/min ECMO flow cannot maintain adequate perfusion in the coronary arteries, causing heart failure. A support for this postulate is provided in Fig. 5(a), which shows the pressure in the right ventricle, and indicates a heart failure at 2.5 L/min. We have not measured the pressure in the left ventricle because the placement of the pressure catheter causes additional shadows to the echo images. Subsequently, as the ECMO flow is lowered to 1.5 L/min, the heart rate increases to maintain a VTI of 120 cm/min, compensating for the persistent decrease in VTI_{stroke}. Based on this discussion, an ECMO flow rate of 3.0 L/min seems to be the minimum level required for maintaining adequate end-organ perfusion for the current severe cardiac injury model.

4   Conclusion

The current study investigates the interaction between cardiac outflow from a severely injured pig's heart with the backflow induced by VA ECMO support system. Our objective is introducing a methodology for using the measured flow structure and parameters derived from it to assess the optimal ECMO flow rate. Time-resolved echo PIV/PTV is performed to characterize the hemodynamic parameters of the flow inside the pig's ascending aorta noninvasively. A series of new procedures are introduced to enhance the echo images prior to velocity calculations. First, a blind deconvolution approach is used to estimate the spatially varying point spread function and utilize it for deblurring the images. This step achieves more prominent intensity peaks in the center of traces and sharper boundaries between adjacent ones. Second, the spatiotemporal variant background is estimated and subtracted from each pixel by choosing the minimum intensity among images filtered spatially at different window sizes. Finally, an active and iterative contouring method is used for masking out undesired sections of images containing tissues and dynamic aortic valve. This process involves the automatic generation of specific masks for each phase of the cardiac cycle. The velocity distribution is computed using a previously developed integrated and optimized procedure encompassing image enhancement, PIV, and PTV. The phase-averaged velocity and vorticity distributions reveal the evolution of flow structure in the ascending aorta, as the ECMO flow interacts with the cardiac outflow. For flow rates above 3.0 L/min, the penetration of ECMO

backflow is observed shortly after the aortic valve closing. Subsequently, a counterrotating vortex pair forms in the sinus, with the transition to the backflow occurring 0.8-1cm downstream the sinotubular junction. When the ECMO flow rate decreases from 4.0 to 3.0 L/min, the maximum cardiac ejection velocity increases, and its location migrates downstream. Finally, surrogates for the cardiac output per cycle and overall flow rate are introduced. Both show a sharp decrease in cardiac function of the severely injured heart when the ECMO flow decreases below 3.0 L/min. Future studies will determine whether this observation could be generalized.

Acknowledgment

References

Abe H, Caracciolo G, Kheradvar A, Pedrizzetti G, Khandheria BK, Narula J, and Sengupta PP (2013) Contrast Echocardiography for Assessing Left Ventricular Vortex Strength in Heart Failure: A Prospective Cohort Study. *European Heart Journal Cardiovascular Imaging* 14:1049-1060

Agati, L, Cimino S, Tonti G, Cicogna F, Petronilli V, De Luca L, Iacoboni C, and Pedrizzetti G (2014) Quantitative Analysis of Intraventricular Blood Flow Dynamics by Echocardiographic Particle Image Velocimetry in Patients with Acute Myocardial Infarction at Different Stages of Left Ventricular Dysfunction. *European Heart Journal - Cardiovascular Imaging* 15:1203-1212

Burkhoff D, Sayer G, Doshi D, and Uriel N (2015) Hemodynamics of Mechanical Circulatory Support. *Journal of the American College of Cardiology* 66:2663-2674

Chan TF, and Vese LA (2001) Active contours without edges. *IEEE Transactions on image processing* 10:266-277

Faludi R, Szulik M, D'hooge J, Herijgers P, Rademakers F, Pedrizzetti G, and Voigt JU (2010) Left Ventricular Flow Patterns in Healthy Subjects and Patients with Prosthetic Mitral Valves: An in Vivo Study Using Echocardiographic Particle Image Velocimetry. *The Journal of Thoracic and Cardiovascular Surgery* 139:1501-1510

Goertz DE, de Jong N, and van der Steen AFW (2007) Attenuation and Size Distribution Measurements of Definity™ and Manipulated Definity™ Populations. *Ultrasound in Medicine & Biology* 33:1376-1388

Keane RD, Adrian RJ, and Zhang Y (1995) Super-Resolution Particle Imaging Velocimetry. *Measurement Science and Technology* 6:754-768

Kim HB, Hertzberg JR, and Shandas R (2003) Development and Validation of Echo PIV. *Experiments in Fluids* 36:455-462

Lawler PR, Silver DA, Scirica BM, Couper GS, Weinhouse GL, and Camp PC (2015) Extracorporeal Membrane Oxygenation in Adults With Cardiogenic Shock. *Circulation* 131:676-680

Makdisi G and Wang IW (2015) Extra Corporeal Membrane Oxygenation (ECMO) Review of a Lifesaving Technology. *Journal of Thoracic Disease* 7:E166-E176

Maska M, Danek O, Garasa S, Rouzaut A, Munoz-Barrutia A, and Ortiz-de-Solorzano C (2013) Segmentation and Shape Tracking of Whole Fluorescent Cells Based on the Chan–Vese Model. *IEEE Transactions on Medical Imaging* 32:995-1006

Osher S, and Sethian JA (1988) Fronts propagating with curvature-dependent speed: algorithms based on Hamilton-Jacobi formulations. *Journal of computational physics* 79:12-49

Ostadal P, Mlcek M, Kruger A, Hala P, Lacko S, Mates M, Vondrakova D, Svoboda T, Hrachovina M, Janotka M, Psotova H, Strunina S, Kittnar O, and Neuzil P (2015) Increasing Venoarterial Extracorporeal Membrane Oxygenation Flow Negatively Affects Left Ventricular Performance in a Porcine Model of Cardiogenic Shock. *Journal of Translational Medicine* 13:1-8

Otsu N (1979) A Threshold Selection Method from Gray-Level Histograms. *IEEE Transactions on Systems, Man, and Cybernetics* 9:62-66

Pan J, Hu Z, Su Z, and Yang MH (2014) Deblurring text images via L0-regularized intensity and gradient prior. In *the IEEE Conference on Computer Vision and Pattern Recognition, Columbus, Ohio, USA, June 23-28*

Pavlushkov E, Berman M, and Valchanov K (2017) Cannulation Techniques for Extracorporeal Life Support. *Annals of Translational Medicine* 5:70

Roth GI and Katz J (2001) Five Techniques for Increasing the Speed and Accuracy of PIV Interrogation. *Measurement Science and Technology* 12:238-245

Sampath K, Harfi TT, George RT, and Katz J (2018) Optimized Time-Resolved Echo Particle Image Velocimetry– Particle Tracking Velocimetry Measurements Elucidate Blood Flow in Patients With Left Ventricular Thrombus. *Journal of Biomechanical Engineering* 140:041010

Sheng J, Malkiel E, and Katz J (2008) Using Digital Holographic Microscopy for Simultaneous Measurements of 3D near Wall Velocity and Wall Shear Stress in a Turbulent Boundary Layer. *Experiments in Fluids* 45:1023-1035

Viessmann OM, Eckersley RJ, Christensen-Jeffries K, Tang MX, and Dunsby C (2013) Acoustic Super-Resolution with Ultrasound and Microbubbles. *Physics in Medicine and Biology* 58:6447-6458

Whyte O, Sivic J, and Zisserman A (2014) Deblurring Shaken and Partially Saturated Images. *International Journal of Computer Vision* 110:185-201